

Multifrequency Radio Observations of the Magnetar Swift J1818.0–1607

EVAN F. LEWIS,^{1,2} HARSHA BLUMER,^{1,2} RYAN S. LYNCH,³ AND MAURA A. McLAUGHLIN^{1,2}

¹*West Virginia University, Department of Physics and Astronomy, P. O. Box 6315, Morgantown, WV 26506, USA*

²*Center for Gravitational Waves and Cosmology, West Virginia University, Chestnut Ridge Research Building, Morgantown, WV 26506, USA*

³*Green Bank Observatory, P.O. Box 2, Green Bank, WV 24944, USA*

Submitted to ApJ

ABSTRACT

We report on Green Bank Telescope observations of the radio magnetar Swift J1818.0–1607 between 820 MHz and 35 GHz, taken from six to nine months after its 2020 March outburst. We obtained multi-hour observations at six frequencies, recording polarimetric, spectral, and single-pulse information. The spectrum peaks at a frequency of 5.4 ± 0.6 GHz, making Swift J1818.0–1607 one of many radio magnetars which exhibit a gigahertz-peaked spectrum (GPS). The radio flux decays steeply above the peak frequency, with in-band spectral indices $\alpha < -2.3$ above 9 GHz. The emission is highly ($> 50\%$) linearly polarized, with a lower degree ($< 30\%$) of circular polarization which can change handedness between single pulses. Across the frequency range of our observations, the time-integrated radio profiles share a common shape: a narrow “pulsar-like” central component flanked by “magnetar-like” components comprised of bright, spiky subpulses. The outer profile components exhibit larger degrees of flux modulation and flatter spectral indices when compared to the central pulse component.

1. INTRODUCTION

Magnetars are a subclass of neutron stars characterized by their large inferred surface magnetic field strengths ($> 10^{14}$ G) and long rotation periods (> 1 s) (Kaspi & Beloborodov 2017). Most magnetars are discovered through their X-ray and gamma-ray outbursts, with burst luminosities exceeding the spin-down luminosity available from the conversion of rotational angular momentum, which is the energy source for the majority of pulsars. Magnetar emission is instead likely powered by the decay of these extreme internal magnetic fields (Duncan & Thompson 1992).

Pulsed radio emission has only been detected from six magnetars¹ including the most recent discovery, Swift J1818.0–1607. In the radio band, magnetar emission tends to be highly linearly polarized, with a flat polarization position angle (PPA) sweep across the center of the profile (Kramer et al. 2007). The emission is composed largely of short, spiky ‘sub-pulses’ falling within

a larger pulse envelope (Levin et al. 2012). Magnetar emission can possess flat or even inverted spectral indices over large intervals of the radio spectrum, as in the case of XTE J1810–197 (Eie et al. 2021; Torne et al. 2022) and the Galactic center magnetar SGR J1745–2900 (Torne et al. 2015, 2017). This is at odds with the majority of rotation-powered pulsars, whose flux follows power-law spectra with an average spectral index of -1.6 (Jankowski et al. 2018).

A unifying feature in magnetar emission across all bands is its temporal variability; particularly in the initial days to weeks after the onset of an outburst, there can be drastic changes in the shape and polarization properties of the integrated radio pulse profile, the overall shape of the spectrum, and single-pulse properties of the radio emission (e.g. Camilo et al. 2016; Scholz et al. 2017; Pearlman et al. 2018; Lower et al. 2023). Large degrees of variability in the spin-down rate of the star are common, and magnetars also exhibit discrete glitching events and pulse profile changes suggestive of a rapidly changing magnetosphere (Lower et al. 2021; Rajwade et al. 2022). Magnetars have also been suggested as a central engine powering some extragalactic fast radio bursts (FRBs), particularly following the detection of FRB-like bursts from the Galactic magne-

Corresponding author: Evan F. Lewis
eff0003@mix.wvu.edu

¹ <https://www.physics.mcgill.ca/~pulsar/magnetar/main.html>

tar SGR 1935+2154 (CHIME/FRB Collaboration et al. 2020; Bochenek et al. 2020). The underlying mechanisms of radio magnetar emission can provide valuable information to understand the FRB population as well as the properties of the magnetospheres surrounding neutron stars.

Swift J1818.0–1607 (hereafter J1818) was discovered on 12 March 2020 when the *Swift*-Burst Alert Telescope detected a 0.01-s duration gamma-ray burst (Evans et al. 2020; Stamatikos et al. 2020). A 1.36-s periodicity was subsequently detected with NICER (Enoto et al. 2020). Within two days of the X-ray outburst, observations with the Lovell and Effelsberg radio telescopes yielded coherent radio pulsations, making J1818 the sixth known radio-loud magnetar as well as the fastest-spinning member of the magnetar population (Karuppusamy et al. 2020; Rajwade et al. 2020).

Like other radio magnetars, J1818 exhibits changes in the shape and number of components in its integrated profile, high degrees of linear polarization, a variable spin-down rate, and flux variability across a range of timescales (Lower et al. 2020; Huang et al. 2021; Rajwade et al. 2022). Its X-ray properties post-outburst were also reminiscent of other magnetar outbursts (Blumer & Safi-Harb 2020; Hu et al. 2020). More recently, the radio flux of J1818 increased from 2022 December to 2023 March, but subsequently decayed, and no detections have been published since then, suggesting J1818 may have entered a quiescent period after its outburst (Ding et al. 2024).

The spin-down luminosity of J1818 is the highest of all magnetars, and higher than its quiescent X-ray luminosity (Hu et al. 2020). Furthermore, the initial radio spectrum of J1818 was markedly steep (Maan & van Leeuwen 2020; Lower et al. 2020), but gradually flattened post-outburst (Majid et al. 2020). Similar spectral behavior was seen in PSR J1119–1627, a seemingly rotation-powered pulsar which has previously exhibited magnetar-like outbursts (Archibald et al. 2016; Dai et al. 2018). These properties are shared with rotation-powered pulsars and not radio magnetars, leading previous authors to speculate that J1818 may represent an evolutionary link between pulsars and magnetars (Hu et al. 2020).

In this paper we detail observations of J1818 taken between 2020 August and 2020 December, ranging in observing frequency from 820 MHz to 35 GHz. Section 2 describes the observations and data reduction. The time-averaged properties of the profile and spectrum are described in Section 3, and the single-pulse properties are described in Section 4. We discuss these

Table 1. Observations

Start Date	MJD	F_c	$\Delta\nu$	N_{chan}	t_{samp}	Length
		(GHz)	(GHz)		(μ s)	(hr)
2020 Aug 31	59092	6.00	4.50	3072	87.38	3.4
2020 Sep 27	59119	35.12	3.75	5118	87.38	1.2
2020 Oct 29	59151	0.82	0.20	128	10.24	1.6
2020 Oct 30	59152	9.11	2.25	1536	87.38	1.1
2020 Nov 20	59173	21.94	7.87	5376	87.38	1.4
2020 Dec 07	59190	13.69	3.37	2304	87.38	1.4

NOTE—Parameters for each observation of Swift J1818.0–1607 as described in the text. F_c denotes the central frequency of the observation, $\Delta\nu$ the bandwidth, N_{chan} the total number of frequency channels, and t_{samp} the native sampling time.

results and their relation to the magnetar and pulsar population in Section 5, and conclude in Section 6.

2. OBSERVATIONS AND DATA REDUCTION

We conducted observations of J1818 using the VEGAS backend on the Green Bank Telescope from August to December of 2020. Details of each observation are presented in Table 1. We began each observation with on- and off-source scans of the standard flux calibrator J1445+0958 (OQ172) while firing the pulsed noise diode.

Except for the 6 and 13-GHz datasets, we also recorded full polarimetric information for each observation. User error prevented the full Stokes parameters from being recorded for the 6-GHz observation, so only total intensity data are available. Furthermore, the noise diodes for the 13-GHz backend were not set up to accurately record full Stokes parameters at the time of our observation, so those data are also summed to total intensity in this study.

As with other magnetars, the spin-down rate of J1818 varied substantially within the first year since its outburst (Champion et al. 2020; Rajwade et al. 2022). Given these fluctuations and the sparse cadence of our observations, we did not create a timing model which spanned our entire dataset. We used the `prepfold` command from the `PRESTO`² (Ransom 2001) software package to fold each observation at the nominal pulsar period of 1.364 s and dispersion measure (DM) of 706 pc cm^{−3} (Karuppusamy et al. 2020; Maan & van Leeuwen 2020),

² <https://github.com/scottransom/presto>

and searched over a range of pulse periods to maximize the signal-to-noise (S/N) of the folded pulse profile.

Instances of terrestrial radio frequency interference (RFI) were identified and excised using the `paz` and `pazi` routines. Frequency channels contaminated with continuous, narrowband RFI throughout the entire observation were excised, as well as individual subintegrations dominated by impulsive, broadband RFI signals. After RFI mitigation, each observation was folded and split into 16 subintegrations, and averaged in frequency to create 16 pulse profiles. Using PRESTO, we generated times of arrival (TOAs) by cross-correlating the total integrated profile with the profile from each subintegration. The TOAs were passed to TEMPO2³ (Hobbs et al. 2006), where we created a basic timing model using the DE405 ephemeris and the known sky coordinates, fitting only for the spin period.

We generated PSRFITS archives of each observation by folding the search-mode data at the best-fit period using DSPSR. The data were polarization- and flux- calibrated using PSRCHIVE⁴ (van Straten et al. 2011). We note that for the 6-GHz observation taken on MJD 59092, only total intensity data were recorded. Archives with full single-pulse information were also saved for analysis; the single-pulse analysis is detailed in Section 4.

In order to correct for the Faraday rotation, we applied a fiducial rotation measure (RM) of 1442 rad m^{-2} , as found in previous studies (Lower et al. 2020). To confirm the validity of this RM within our dataset, we fit for the Faraday rotation measure with the PSRCHIVE routine `rmfit` on the 800 MHz observation, which returned a best-fit RM of $1444 \pm 0.2 \text{ rad m}^{-2}$. Given that `rmfit` may underestimate the error bars on these measurements (e.g. Wahl et al. (2022)), we determined that the fiducial RM of 1442 rad m^{-2} was sufficient.

3. PROFILE AND SPECTRAL EVOLUTION

3.1. Time-Averaged Pulse Profiles

Figure 1 displays the time- and frequency-integrated pulse profile of the magnetar at each observing frequency. Above a frequency of 1 GHz, the integrated profiles are made up of three distinct components: a precursor (I), narrow main component (II), and wider post-cursor (III). Due to our lack of a phase-connected timing solution, the profiles are all aligned so that the peak of Component II occurs at a rotational phase of

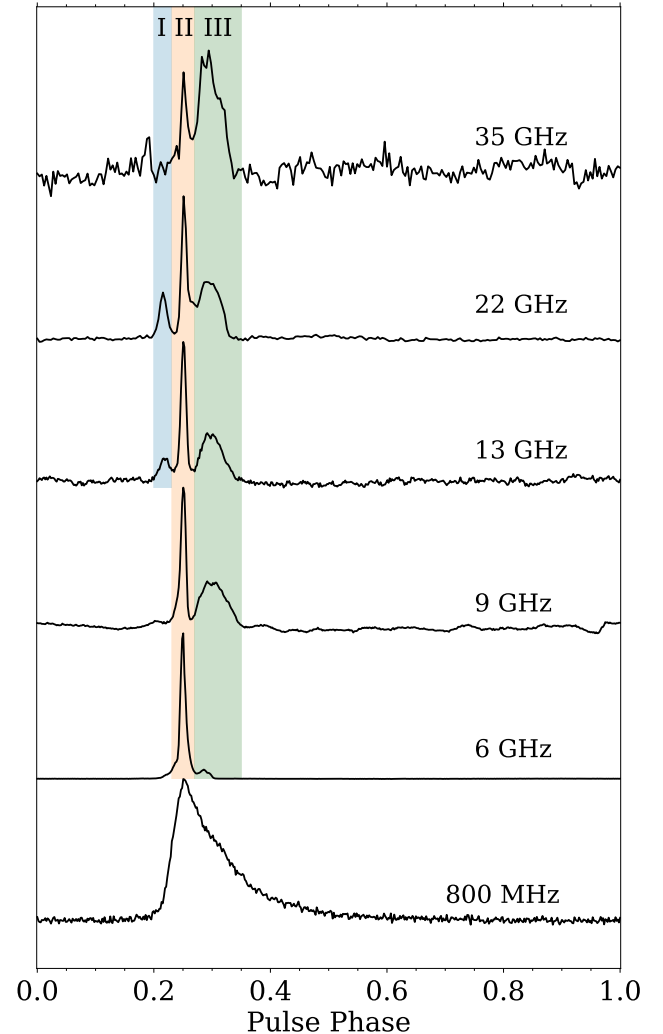


Figure 1. The total intensity profile of J1818 at each observing frequency. Each profile covers one full rotation of the magnetar and is divided into the number of bins which maximizes the profile S/N. For visual clarity, each profile component is highlighted where present: component I in blue, component II in orange, and component III in green.

0.25; the 820-MHz profile is aligned so that its peak occurs at the same phase.

To measure the full-width half-maximum (FWHM) pulse width of each profile component, we used `scipy.optimize.curve_fit` to model each component with a single Gaussian function. The resulting pulse widths are reported in Table 2. We also calculate the on-pulse flux of the linearly- and circularly-polarized data, and present the linear polarization fraction (L/I) and circular polarization fraction (C/I) of each component.

The 820-MHz profile is dominated by scatter broadening. The NE2001 electron-density model predicts a

³ <https://www.atnf.csiro.au/research/pulsar/tempo2/>

⁴ <https://psrchive.sourceforge.net>

Table 2. Pulse component properties

Frequency (GHz)	Pulse Width (FWHM)			α			L/I			C/I		
	I	II	III	I	II	III	I	II	III	I	II	III
0.82				54.5(7)				9(3)
6.00	(a)	16.0(1)	33.4(4)	(a)	(b)	(b)		(c)				(c)
9.11	(a)	15.8(2)	74.9(6)	(a)	-3.3(5)	-2.6(4)	(a)	60(10)	20(11)	(a)	29(9)	...
13.69	37.6(5)	15.9(1)	65.0(3)	-2(2)	-2.3(6)	-2.1(4)		(c)				(c)
21.94	23.6(4)	17.4(6)	63(1)	-3(2)	-3.4(8)	-3.4(6)	70(15)	60(5)	65(3)	...	25(17)	20(17)
35.12	(a)	34(2)	59(1)		...		(a)	...	42(16)	(a)

NOTE—Fitted full-width half-maximum (FWHM) pulse widths, spectral indices, linear polarization fractions, and circular polarization fractions for the three profile components depicted in Figure 1. The $1-\sigma$ error bars are denoted by parentheses on the last significant digit. We only present values for profile components which are detected significantly enough to reliably measure these properties. The 820-MHz profile is not divided into distinct components: the linear and polarization fractions are calculated over the entire range of the pulse profile.

^aProfile component not significantly detected.

^bNot well-fit by a simple power law; see Section 3.2.

^cPolarization calibration not available for this observation.

scattering timescale⁵ of 61 ms Cordes & Lazio 2002). An alternative approach is to use the empirical relation between DM and scattering timescale; this results in a prediction of 72 ms at that frequency (Yao et al. 2017). We estimated the scattering timescale by fitting to the 820-MHz integrated profile a Gaussian function convolved with a one-sided exponential broadening function, and scaled to 1 GHz assuming a frequency dependence of $\tau_s \sim \nu^{-4.4}$. The best-fit scattering timescale of 46 ± 4 ms is in agreement with the previously measured $\tau_s = 42_{-3}^{+9}$ ms (Lower et al. 2020) and 44 ± 3 ms (Champion et al. 2020). Above frequencies of 6 GHz, the scattering timescale is predicted to be less than 10 ns and the effects of scattering can be ignored.

The polarization position angle (PA) of the linear polarization, Ψ , is shown for each observation in the top panel of Figure 2. Variations in the PA with pulse phase can be explained with the rotating vector model (RVM); the RVM models the pulsar magnetic field as a simple dipole, in which case the PA ‘sweep’ across the radio profile is caused by the changing angle between the magnetic axis and our line of sight (Radhakrishnan & Cooke 1969). In this simple case, the RVM predicts a flat, S-shaped sweep in PA across the pulse profile.

We observe mostly flat PA swings across the phase range of the integrated pulse profiles, especially at 820

MHz, in line with the early low-frequency detections of J1818 (Champion et al. 2020; Lower et al. 2020). The PA swing of the 22 GHz observation is much steeper, and inverted with respect to the other observations, but still retains the characteristic S-shaped sweep if a small offset is added to the position angles in Figure 2. Similar changes in the polarization properties of J1818 were seen at 2.6 GHz by Lower et al. (2021), in which case the PA exhibited a steeper, reversed PA sweep on a single epoch of observation before returning to a positive slope.

The spectral properties of the individual components are further discussed in Section 3.3, and single-pulse properties in Section 4.

3.2. Flux Density and Spectral Indices

Figure 2 shows the time-integrated frequency/phase plots, spectral fits, polarization profiles, and linear polarization position angles for each observation in which the magnetar was detected. We see no evidence of astrophysical scintillation in our dataset. Below 22 GHz, the scintillation bandwidth predicted by the NE2001 model is smaller than the bandwidth of a single frequency channel. The scintillation bandwidth predicted by the NE2001 model is 2.4 MHz in the 22-GHz observing band, and 19 MHz in the 35-GHz observing band. Therefore, even though just resolvable, it would be difficult to detect scintillation with sufficient signal-to-noise at these frequencies.

⁵ Calculated using <https://apps.datacentral.org.au/pygedm/>

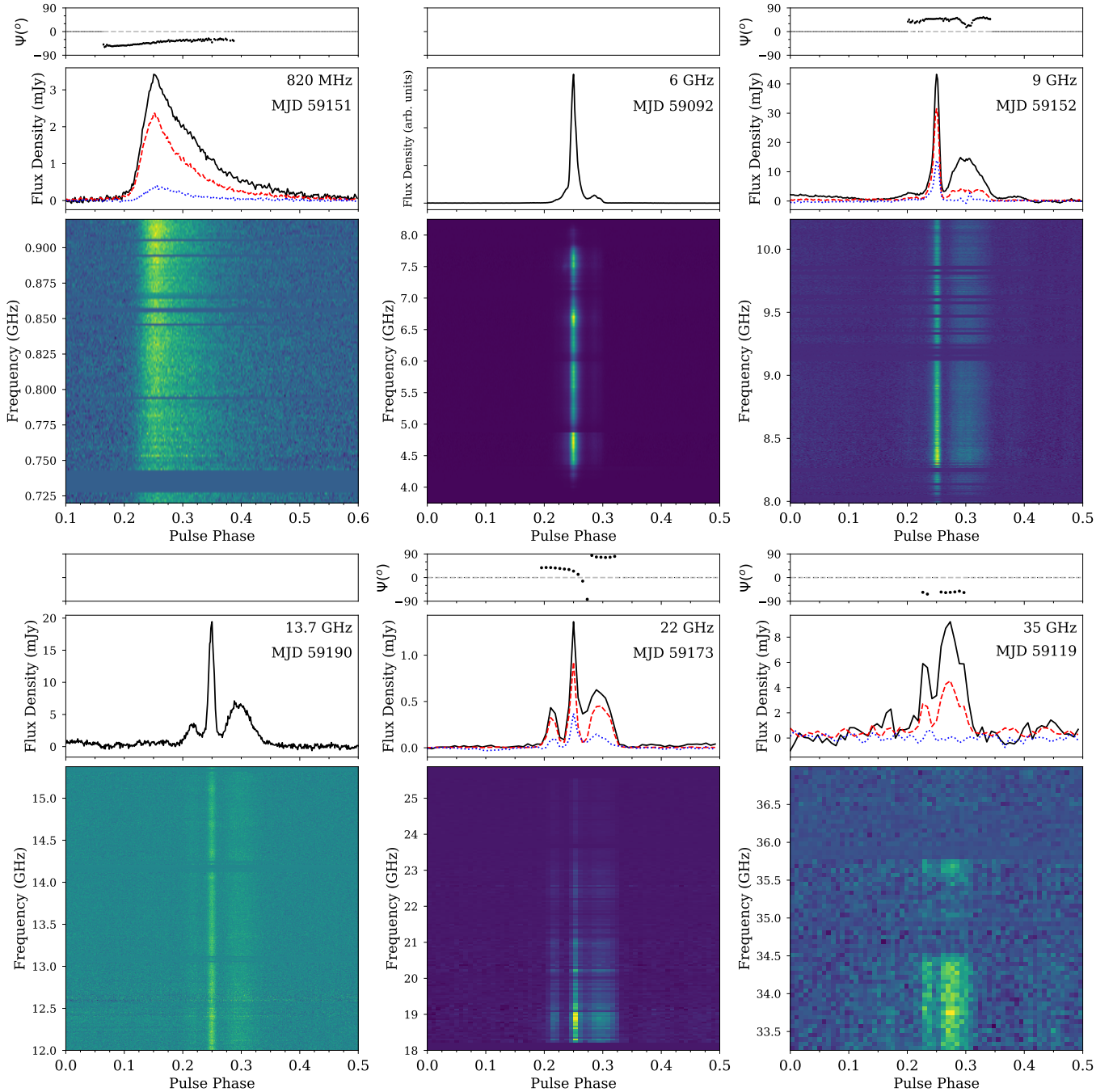


Figure 2. For each observation of J1818, we show the polarization position angle sweep (top panel), calibrated polarization profile with total intensity in black, linear polarization in red, and circular polarization in blue (middle panel), and frequency-phase plot (bottom panel). Polarization information is not available for the 6- and 13-GHz data.

In order to measure the flux density of the source at each observing frequency, each observation was time-integrated and split into at most 16 subbands to produce a one-dimensional pulse profile for each subband.

The number of subbands was chosen such that the measured flux density was greater than its corresponding error in each subband; higher-significance flux mea-

surements would have necessitated using too few subbands to get good fits. The mean flux density S in each subband is given by

$$S = \frac{1}{N_b} \sum_{i=0}^{N_b} S_i, \quad (1)$$

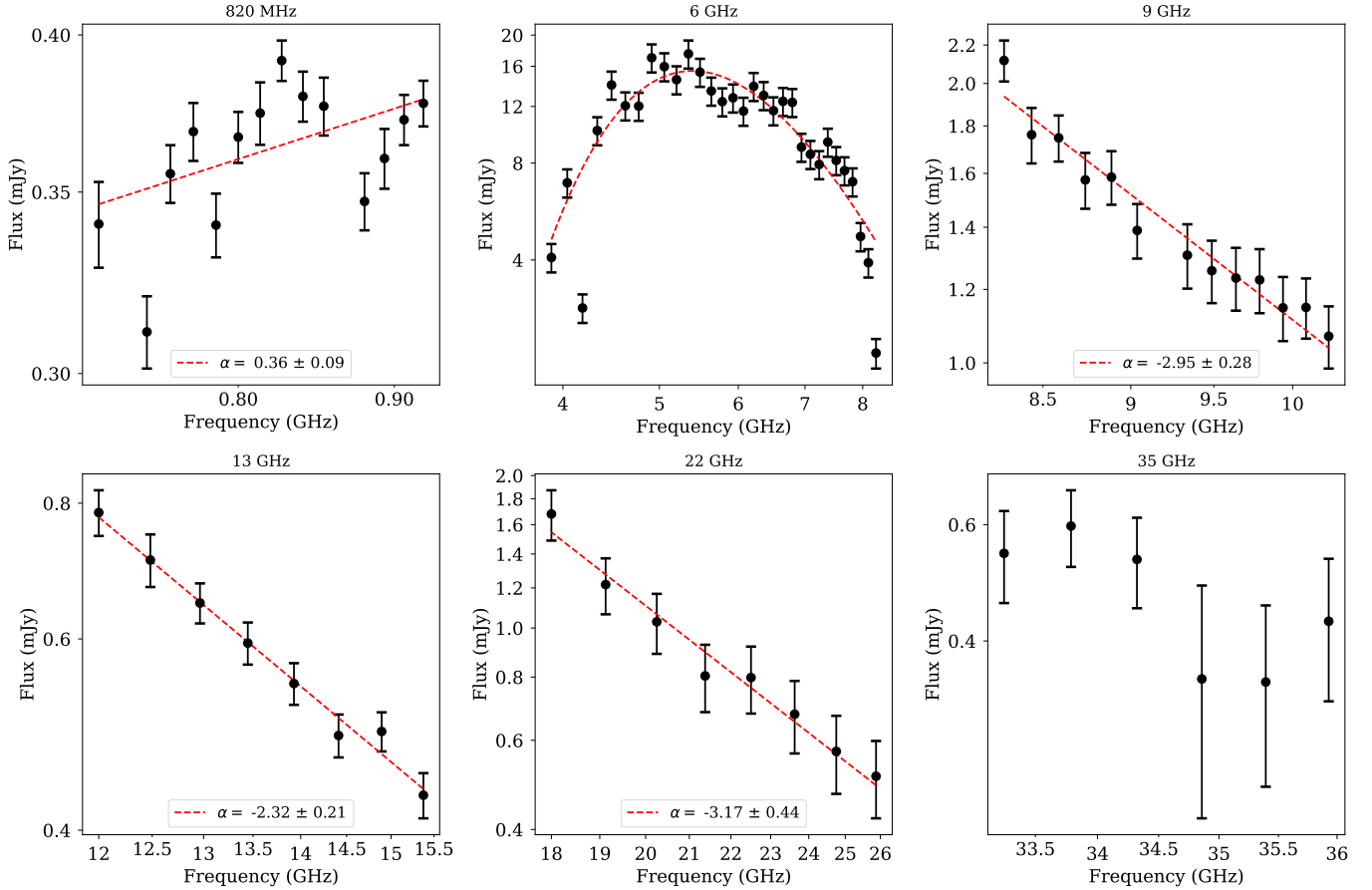


Figure 3. The flux measurements in each subband and their corresponding errors are shown in black. The best-fit power law is overlaid in red, with the associated spectral index and 1- σ error at the bottom of each panel. The 6-GHz data are fit with a combined power-law and free-free absorption spectral model (see text). No spectral index was obtained when fitting the 35-GHz data.

where N_b is the number of bins in the profile, and S_i is the flux density in bin i . We first subtract the off-pulse mean from each profile, so this method is equivalent to summing over only the on-pulse phase bins. The on-pulse phase window is defined using the phase ranges 0.2 to 0.35, except for the 820-MHz profile, where the on-pulse region is extended to 0.6 to account for scatter broadening. The off-pulse region is defined as the regions not covered by the on-pulse region: phase ranges 0 to 0.2, and 0.35 to 1 (0.6 to 1 for the 820-MHz profile). The corresponding error on each flux density measurement is calculated from the off-pulse root mean square (RMS) divided by the square root of the number of phase bins.

We also summed each observation into a single frequency channel and measured the mean flux of J1818 at that observing frequency; the results are given in Table 3.

Table 3. Spectral indices

Date (MJD)	F_c (GHz)	S_{mean} (mJy)	Freq range (GHz)	α (in band)
59151	0.82	0.359(4)	(0.76, 0.92)	+0.2(1)
59092	6.0	2.56(1)
59152	9.1	1.35(4)	(8.3, 10.2)	-2.9(3)
59190	13.7	0.58(2)	(12.0, 15.3)	-2.2(2)
59173	21.9	0.24(2)	(18.0, 25.9)	-3.2(4)
59119	35.1	0.49(6)

NOTE—The central frequency (F_c) of each observation along with S_{mean} , the phase-averaged mean flux at that frequency. The 1- σ error bars are denoted with parentheses on the last significant digit. The spectral indices from the fits in Figure 3 are also listed along the frequency ranges over which they are measured.

The 6 GHz observation did not have available flux calibration, so we used the radiometer equation to scale each profile into Jansky units using a scaling factor:

$$\frac{T_{\text{sys}}}{\sigma G \sqrt{n_p t_{\text{obs}} \Delta\nu}} \quad (2)$$

The system temperature $T_{\text{sys}} = T_{\text{rec}} + T_{\text{sky}}$, where the receiver temperature $T_{\text{rec}} = 23$ K (“Observing with the GBT”, version 4.0)⁶ and the sky temperature T_{sky} was calculated at the central frequency of each subband using the `pyGDSM` Python interface⁷ for the Zheng et al. (2017) global diffuse sky model. The gain of the GBT is 2 K/Jy (“The Performance of the GBT”)⁸, and the on-source time is taken from Table 1. The bandwidth ($\Delta\nu$) and off-pulse standard deviation (σ) are calculated separately for each subband. We add in quadrature a 10% uncertainty on each flux measurement due to the systematic errors involved in using the radiometer equation, due to uncertainties and time dependence in the gain and system temperature.

Flux measurements of the calibrated 22-GHz observation yielded mean fluxes on the order of 50 μJy , at odds with the high S/N of its integrated profile and the mean flux of J1818 at all other frequencies. We used the radiometer equation as a validity check, assuming a system temperature of 40 K and using the same method described above to estimate the fluxes and their corresponding errors. The radiometer equation returns mean fluxes in the range of 0.1 to 1 mJy, and given that these measurements made more physical sense, we determine that there was an error in the flux calibration, and use the radiometer fluxes from the 22-GHz observation for our analyses.

The evolution of flux with frequency of pulsars is usually described by a power law relationship, with a spectral index α where $S \sim \nu^\alpha$. Since the majority of our spectra in Figure 3 appeared to follow power-law relationships, we fit power-law spectra to those flux measurements using the non-linear least squares fitting method provided by `scipy.optimize.curve_fit`. The flux measurements and their associated spectral fits are shown in Figure 3, and Table 3 reports the measured spectral indices for each observation, with 1- σ error bars. The 35-GHz signal-to-noise ratios in individual subbands were too low to accurately constrain a spectral index.

The 6-GHz spectrum is not defined by a single power law. Given the clear spectral peak within the observing band, and the negative spectral indices at all higher frequencies, we see evidence of a gigahertz-peaked spectrum (GPS) as seen in other magnetars (discussed further in Section 5). To model the spectral behavior, we used a simple power law combined with a free-free absorption model as described in Kijak et al. (2021). The evolution of flux with frequency is modeled as

$$S(\nu) = A \left(\frac{\nu}{\nu_0} \right)^\alpha e^{-B\nu^{-2.1}} \quad (3)$$

where A is the intrinsic flux of the pulsar at a characteristic frequency ν_0 , α is the power-law spectral index, and B is a frequency-independent parameter.

The observed radio spectrum peaks at a frequency of 5.35 GHz. The best-fit model, obtained through least-squares fitting, peaks at a frequency of 5.4 ± 0.6 GHz. The GPS spectral model does not directly fit for a peak frequency, so to estimate an error, we used the 1- σ errors on the spectral fit to find the peak frequency of the models with $\pm 1\sigma$ on the parameters A , α , and B .

The mean flux of J1818 at each frequency is shown in the top panel of Figure 4. The light gray bars denote the frequency ranges of the 9- and 22- GHz datasets, to distinguish them from the other observations. We note that these observations are spread out over the course of roughly 100 days, and given the known flux variability of magnetars over time, these results cannot be used to study the instantaneous broadband spectrum of J1818 nor the time variability of its spectrum.

3.3. Phase-resolved Spectroscopy

In order to better understand the emission properties of the individual profile components, we also measured the time-averaged spectral index of each component. We defined the on-pulse region of each individual component using the highlighted phase ranges in Figure 1, and calculated mean on-pulse fluxes for each component by using only these relevant parts of the profile. We used these on-pulse fluxes to calculate the spectral indices of the individual profile components at each frequency. The mean fluxes of each component are shown in the bottom panel of Figure 4, and the resulting fitted spectral indices are provided in Table 2. Overall, we find that the spectral indices of component II are steeper (more negative) than those of I and III at most frequencies.

4. SINGLE-PULSE ANALYSIS

The single pulses of J1818 demonstrate significant variability in their flux and morphology over time, simi-

⁶ <https://greenbankobservatory.org/portal/gbt/observing/>

⁷ <https://github.com/telegraphic/pygds>

⁸ <https://www.gb.nrao.edu/GBT/Performance/PlaningObservations.htm>

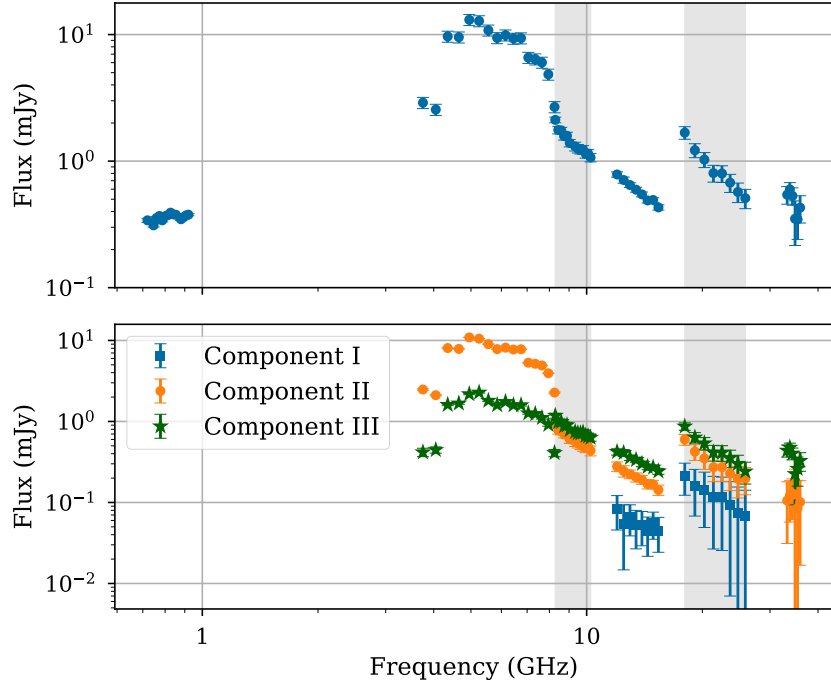


Figure 4. Top: phase-averaged mean flux of J1818 as a function of observing frequency. Bottom: the phase-averaged mean flux of each individual pulse component as a function of observing frequency. The frequency ranges of the 9- and 22-GHz observations are indicated with vertical gray bars to separate them from the other observations.

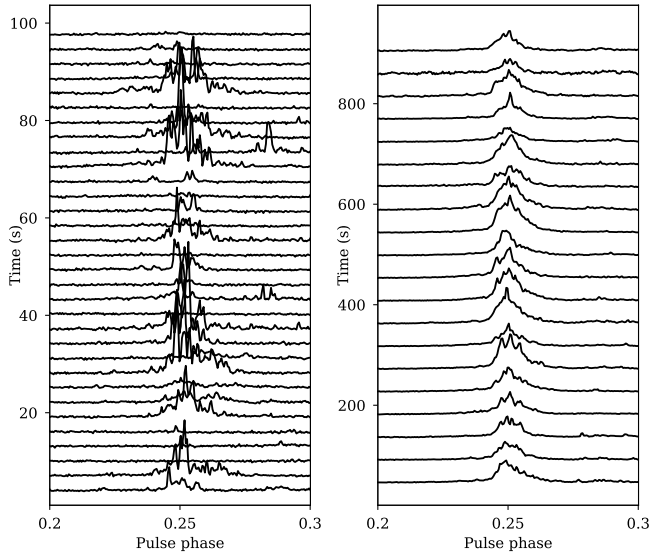


Figure 5. Stacked pulse profiles from the 6-GHz observation of J1818. The pulses are centered at a pulse phase of 0.25 and the horizontal axis covers one tenth of the magnetar’s rotation. Left: 32 consecutive pulses stacked atop one another. Each profile represents one rotation of the magnetar. Right: the change in the integrated profile at 6 GHz over time. Each profile represents 32 rotations of the magnetar, equivalent to 43.6 seconds.

lar to other radio magnetars. For instance, Figure 5 displays 32 consecutive single pulses at 6 GHz, contrasted

Table 4. Single pulse statistics

Date (MJD)	F_c (GHz)	N_{rot}	N_{pulse}	β (hr ⁻¹)	$S_{peak,mean}$ (mJy)
59151	0.82	4269	2314	1450	4.7
59092	6.0	9086	8527	2500	93
59152	9.1	3022	1261	1150	101
59190	13.7	3653	675	480	72
59173	21.9	3745	1282	920	17
59119	35.1	3251	10	~8	...

NOTE—The central frequency (F_c) of each observation along with the number of magnetar rotations covered by our observations (N_{rot}), the number of pulses detected with significance $\sigma \geq 4$ (N_{pulse}), the average detected burst rate (β), and the mean peak flux of all detected ($\sigma \geq 4$) pulses on that epoch. There are too few bright pulses at 35 GHz for a meaningful average.

against the relatively stable pulse profile over the 3.4-hour long observation. A selection of single pulses at 6 GHz and their waterfall plots are also shown in Figure 6. Time-phase plots with 9.55-second (i.e. seven pulses) subintegrations are shown in Figure 7.

4.1. Pulse Energies

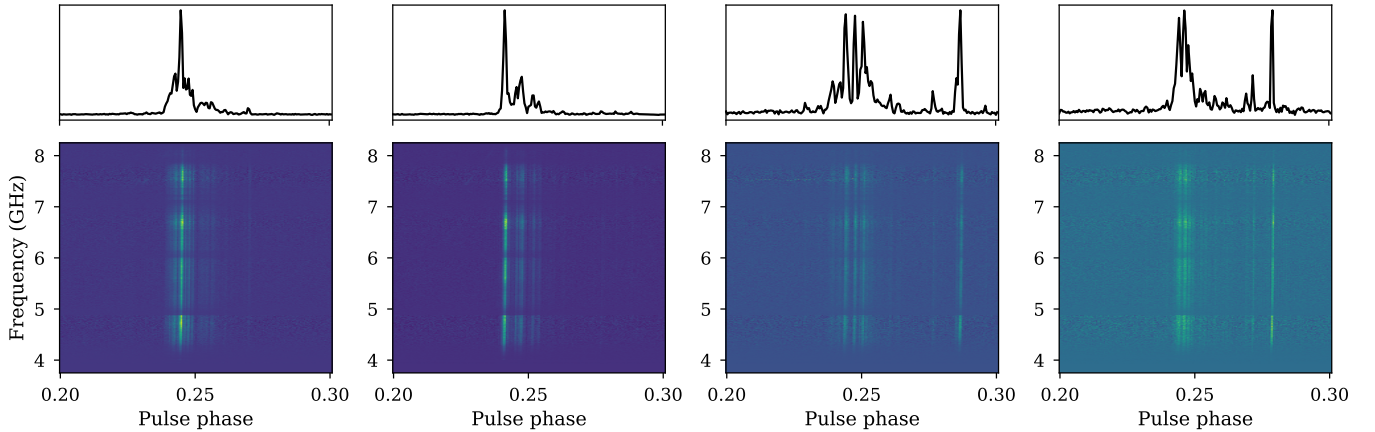


Figure 6. Selected single pulses from the 6-GHz observation. Top panel: the intensity of each single pulse as a function of time. Bottom panel: intensity of the pulse as a function of frequency and time. We show 10% of the full pulse period.

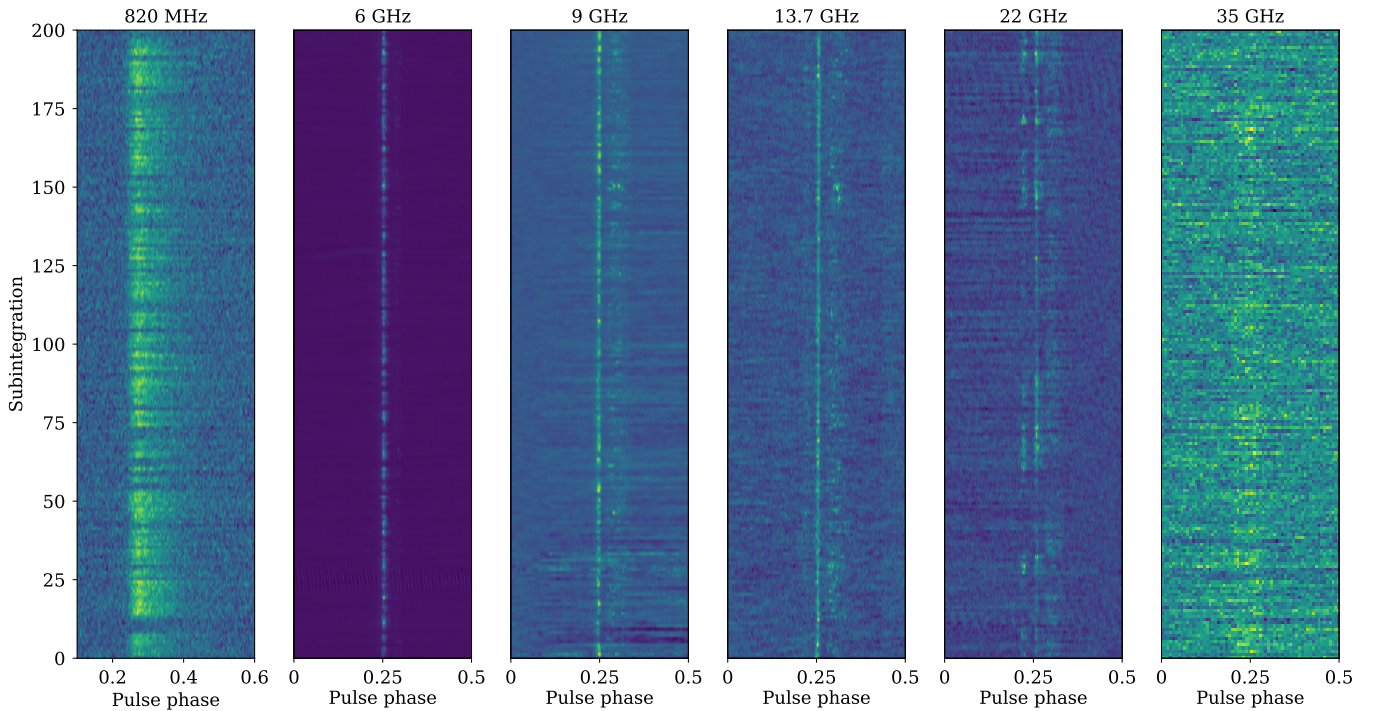


Figure 7. Subintegration pulse stacks of each observation of J1818 analyzed in this work. Each subintegration has a duration of roughly 9.55 seconds, equivalent to seven rotations of the magnetar.

We measured the peak flux of each pulse using the peak amplitude of the on-pulse region. The significance of each pulse was calculated as the peak amplitude divided by the off-pulse standard deviation. Only pulses with significance ≥ 4 were considered. The fluxes of each pulse were normalized by the mean peak flux of all pulses on that epoch.

We fit a log-normal and power-law function to each distribution of pulse fluxes, except for the 35-GHz distribution due to the low number of high-significance single pulses. We fit the power-law distributions to energy

bins past the peak of the distribution. The peak flux distributions and their corresponding fits are shown in Figure 8. At low observing frequencies, the log-normal fits are preferred, with no evidence of a power-law tail. Above 9 GHz, the best-fitting log-normal distribution underestimates the number of high-flux pulses, and the power-law tail fits are preferred, though we note that the power-law fits still overestimate the number of high-flux pulses, especially at 6 and 13 GHz.

Since each single pulse is represented by its peak flux across the on-pulse region, Figure 8 only considers the

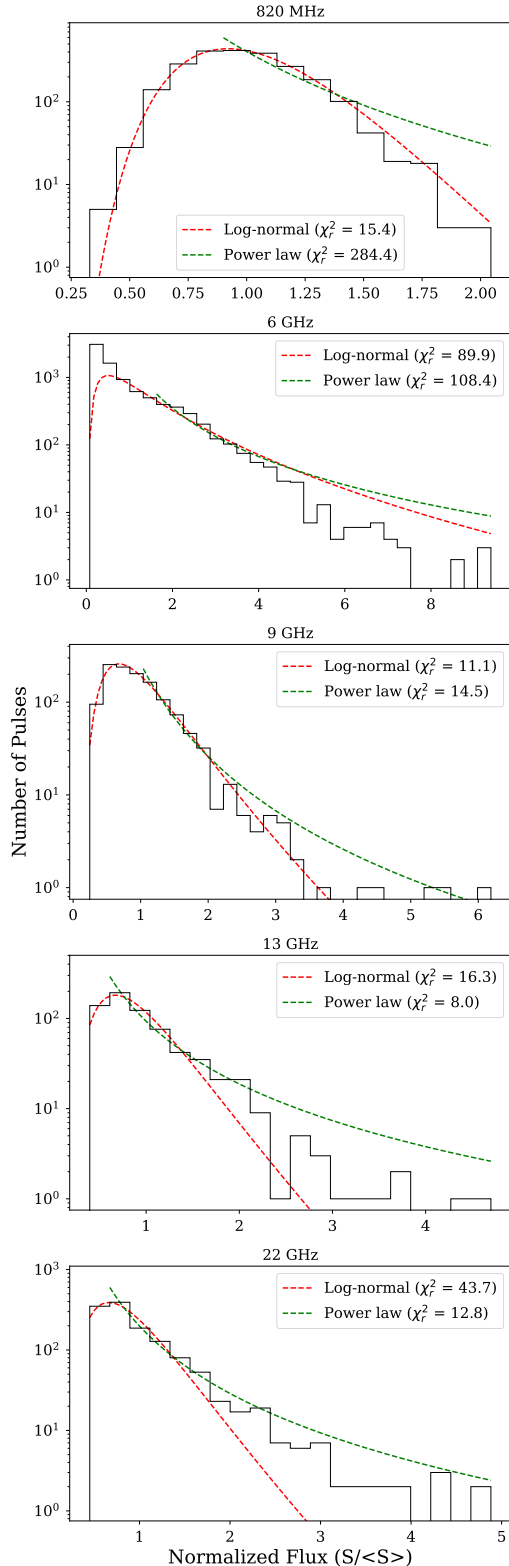


Figure 8. The distributions of phase-averaged peak flux density are shown in black for each observation. The pulse fluxes are normalized by the mean of the peak flux densities of all pulses from that epoch. Overlaid in red are the log-normal (red dashed line) and power-law tail (green dashed line) fits to each distribution. The reduced χ^2 values for each fit are given in the legend. There were not enough high-significance pulses at 35 GHz to fit a distribution.

brightest component within each rotation. We measured the peak flux for each profile component across each rotation of the magnetar, and normalized them by the mean peak flux of that component on that epoch. Figure 9 shows the distribution of pulse energies, separated by pulse component. The only pulses with energies > 10 times the average energy (a typical definition for giant pulses) come from Component III at 6 GHz, for which the power law fit is preferred.

4.2. Flux Modulation

To quantify the temporal variability of each pulse profile component, we calculated the modulation index of each phase bin. We calculate the integrated profile, variance, and the modulation index of each phase bin following the formulation laid out in [Weltevrede et al. \(2006\)](#), which we reproduce here. The value of the mean folded profile, μ_i at bin i , is

$$\mu_i = \frac{1}{N} \sum_{j=0}^N S_{ij} \quad (4)$$

where N is the total number of pulses averaged over, and S_{ij} is the signal intensity in pulse bin i in pulse j . We calculate the variance of intensities within each pulse bin,

$$\sigma_i^2 = \frac{1}{N} \sum_{j=0}^N (S_{ij} - \mu_i)^2 \quad (5)$$

and the modulation index of pulse bin i is then

$$m_i = \frac{\sigma_i}{\mu_i} \quad (6)$$

Figure 10 displays the modulation indices across the on-pulse window of J1818 at each frequency, and Figure 11 displays the modulation indices at 9, 13, and 22 GHz along with pulse stacks.

At each frequency, the modulation index of component II is significantly smaller than those of components I and III, where detected. As seen in the pulse stacks in the bottom panels of Figure 11, the modulation indices suggest that component II would have a relatively consistent intensity over time, and the side components display more infrequent and variable emission, comparable to the narrow, spiky subpulses typical to magnetar emission.

4.3. Polarization

We examined the degree of linear and circular polarization within each single pulse by measuring the polarized flux and comparing it with the flux of the total-intensity pulse. The errors on the linearly and circularly

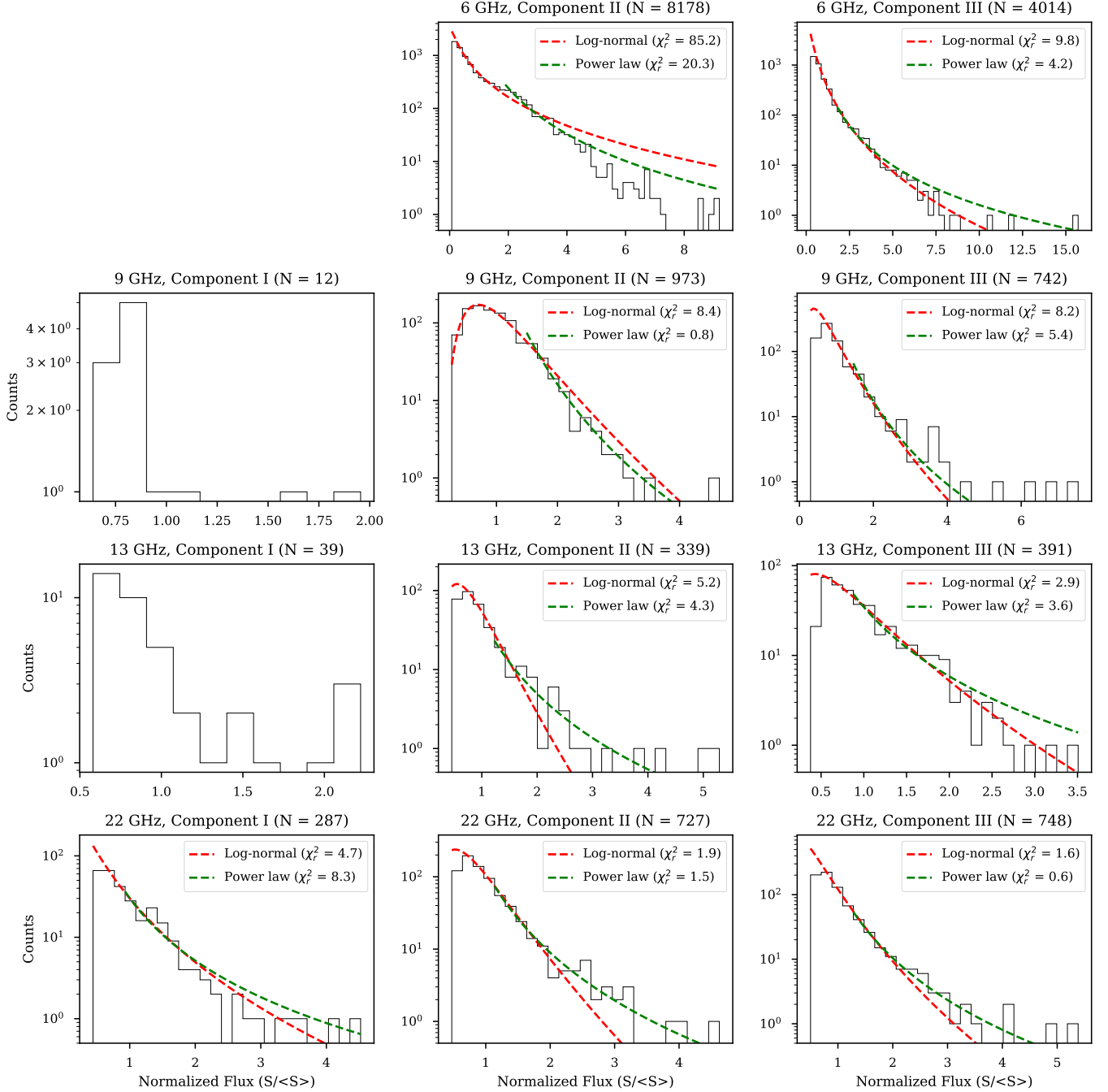


Figure 9. The normalized peak flux distributions of each individual component from 6 to 22 GHz. The x-axis is normalized by the mean peak flux of that individual profile component. Overlaid in red are the log-normal (red dashed line) and power-law tail (green dashed line) fits to each distribution. The reduced χ^2 values for each fit are given in the legend. Fits to the Component I distributions at 9 and 13 GHz failed due to the small number of pulses.

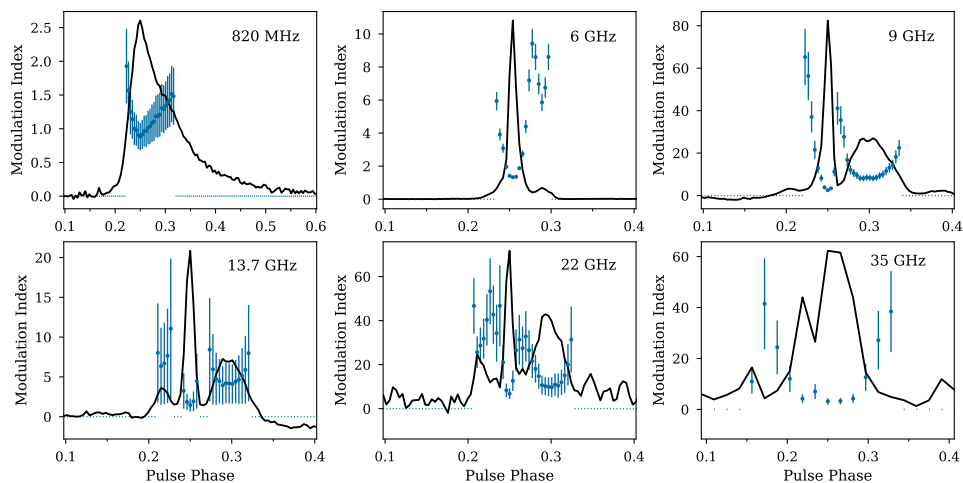


Figure 10. The modulation indices of J1818 as a function of pulse phase at each frequency are shown in blue. The normalized integrated pulse profiles are overlaid in black. Modulation indices are not plotted for phase bins dominated by noise.

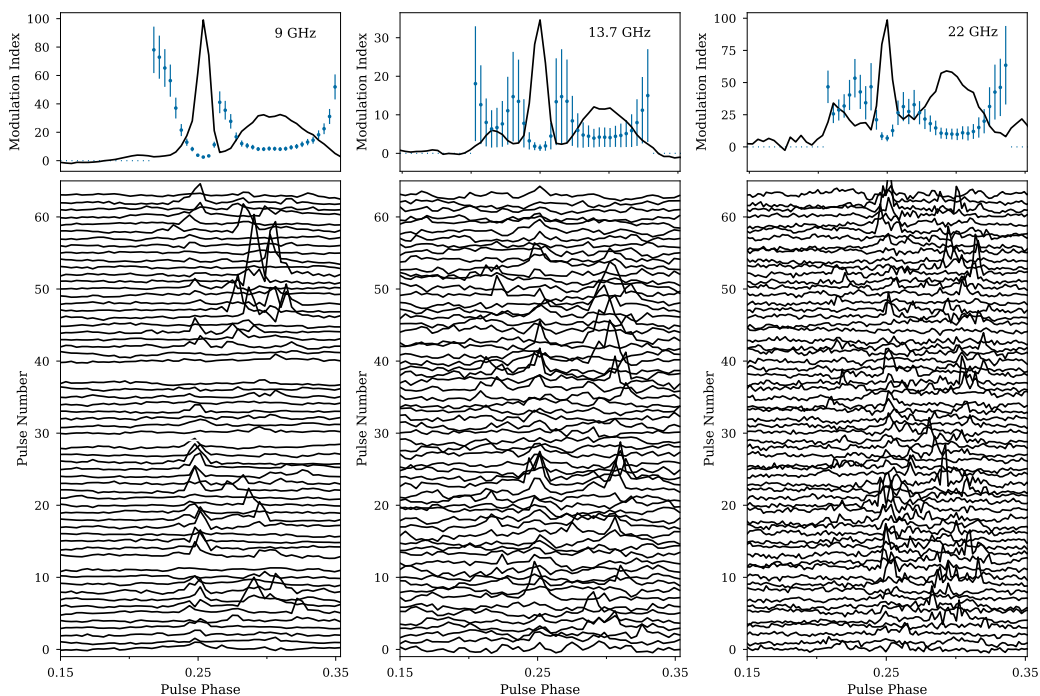


Figure 11. The modulation indices of J1818 at 9, 13, and 22 GHz, with pulse stacks. Top panel: modulation indices are plotted in blue, normalized integrated pulse profiles are overlaid in black. Bottom panel: 64 consecutive single pulses at each frequency. Some pulses have been excised due to RFI corruption.

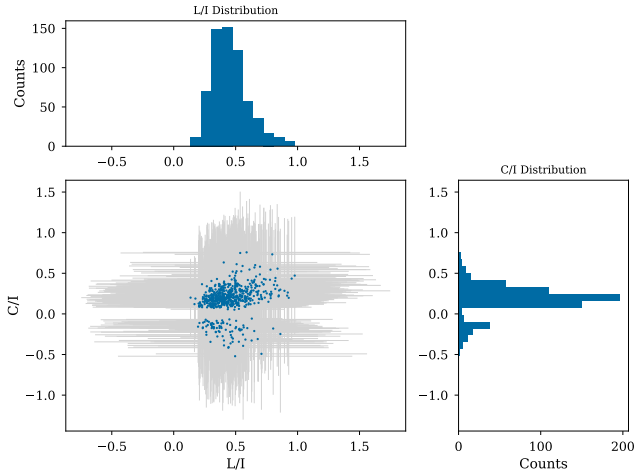


Figure 12. The distribution of linear polarization fraction (L/I) and circular polarization fraction (C/I) for each single pulse at 820 MHz. $1-\sigma$ error bars on each point are denoted in light gray.

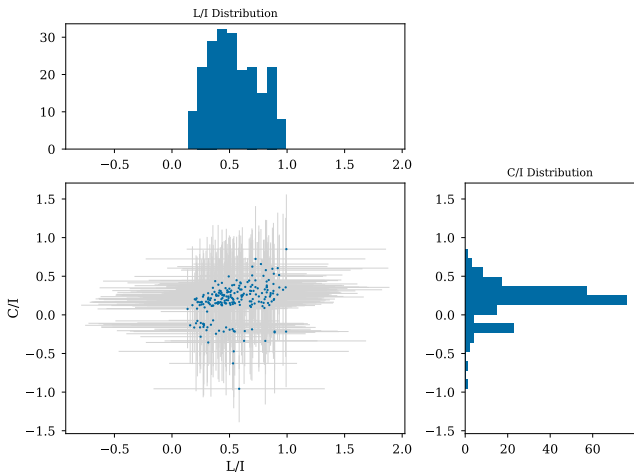


Figure 13. The distribution of linear polarization fraction (L/I) and circular polarization fraction (C/I) for each single pulse at 9 GHz. $1-\sigma$ error bars on each point are denoted in light gray.

polarized fluxes are calculated as the off-pulse RMS of the respective polarized pulse profile (i.e. the RMS of the linearly polarized profile is the error on the linearly polarized flux). To examine the distribution of polarization fractions, we first excised pulses from our sample which had polarized fluxes greater in magnitude than the total-intensity flux and pulses with flux measurement errors larger than the flux measurements themselves.

The resulting distributions of single pulse polarization fractions (linear, L/I , and circular, C/I) at 820 MHz and 9 GHz are respectively shown in Figures 12 and 13. In comparison to the polarization fractions of the time-

integrated profiles given in Table 2, the pulses at 820 MHz have a lower average L/I and higher average C/I . At 9 GHz, the L/I distribution is wider and there are more highly linearly polarized pulses, but the C/I distributions are similar at both frequencies. In both cases, there is a slight positive correlation between L/I and $|C/I|$.

At both frequencies, a portion of the single pulses have the sign of the circular polarization reversed. Pulse-to-pulse changes in the handedness of the circular polarization have been observed before in radio magnetars alongside structures in the PA which deviate significantly from the RVM (Kramer et al. 2007; Dai et al. 2019). Similar behavior was also observed in a long-period radio transient with similar emission properties to FRBs and magnetars (Men et al. 2025). We show some of the 9-GHz single pulses and their PA swings in Figure 14.

4.4. Searches for Periodic Substructure

Across all frequencies, the single pulses from J1818 are comprised of multiple emission components of varying widths and strengths. Even within a single ‘component’ region as described in Section 3.1, there may be several bright, narrow peaks (see e.g. Figures 5, 6, and 11).

The complexity and pulse-to-pulse shape variation discouraged us from attempting a simple FWHM width fit to each pulse component. Instead, we employed an autocorrelation function (ACF) to uncover any underlying quasi-periodicities within the on-pulse emission region of each pulse. Quasi-periodic structure within individual pulses has been suggested as a common feature between all radio-emitting neutron stars, including rotation-powered pulsars and magnetars (Kramer et al. 2024). Though the exact value of the sub-periodicities can vary from pulse to pulse and between epochs, Kramer et al. (2024) found characteristic quasi-periodicities of 2 ms and characteristic sub-pulse widths of 1 ms when examining single pulses from J1818 at observing frequencies between 4 and 8 GHz.

To search for quasi-periodic sub-pulse structure, we first made high-time-resolution timeseries of each observation. Each observation was de-dispersed and written out to a timeseries with 8192 pulse phase bins, equivalent to a $166 \mu\text{s}$ time resolution. The sub-pulse structure resolution is lost at 820 MHz due to dispersive smearing of the pulses, and there was an insufficient number of bright pulses at 35 GHz to perform this analysis.

For the remaining observations, we took an on-pulse cutout covering 20% of the magnetar’s rotation (roughly 275 ms in duration) for each single pulse and took its autocorrelation function. For a given pulse timeseries

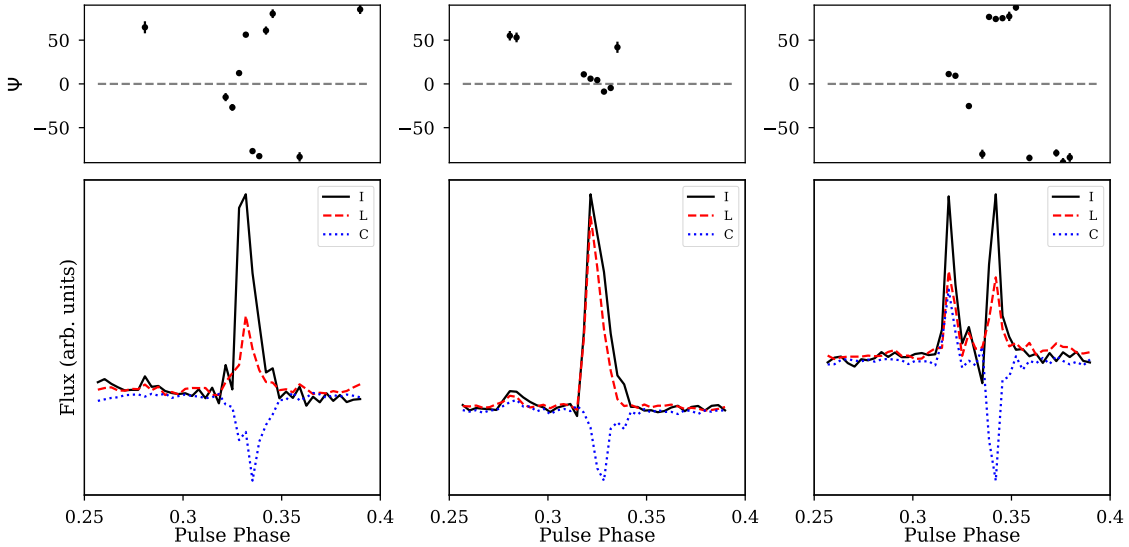


Figure 14. Example single pulses with reversed handedness of circular polarization. Top panels: the polarization position angle, with a gray horizontal dashed line at zero degrees. Bottom panels: the total intensity profile of the single pulse in solid black, linear polarization as a dashed red line, and circular polarization as a dotted blue line.

$I(n)$ with n pulse phase bins, the value of the ACF at a time lag k is given by

$$\text{ACF}(k) = \sum_n I(n+k) * I(n) \quad (7)$$

If there is periodic structure within the subpulses, there will be several equally spaced local maxima in the ACF. The first local maximum corresponds to the fundamental quasi-periodicity, and the rest are harmonics located at multiples of the fundamental period (Lorimer & Kramer 2012; Kramer et al. 2024). Similarly, the characteristic width of the individual subpulses can be determined by measuring the first local minimum preceding the first local maximum.

We chose pulses with peak significance $\sigma \geq 4$ as defined in Section 4.1 to perform the autocorrelation analysis. For each pulse, we calculated the ACF and the Fourier transform of the ACF, and used the `scipy.optimize` implementation of cubic spline fitting to search for local maxima in both the ACF and its Fourier transform. An example pulse with a detected quasi-periodicity of 2.7 ms and its ACF analysis are shown in Figure 15.

Any identified peaks in the ACF or its Fourier transform are saved. At each frequency, we also examined the 100 single pulses with the highest peak significance by eye, and noted any pulses with clear periodically spaced peaks in the ACF, which the cubic spline fitting did not identify.

For each of these pulses and their associated quasi-periodicities, we also wanted to measure a statistical significance for each quasi-periodicity. We took each

pulse with an identified quasi-periodicity and randomly scrambled the order of its phase bins 1000 times. We took the ACF of each scrambled pulse and identified the maximum value outside of the first and last bin (e.g. the quasi-periodicity of the simulated pulse), and summed the values of the ACF at the maximum value and its harmonics. The simulated ACF sums form a null distribution, and the mean and standard deviation of this distribution can be compared to the summed ACF power of the real quasi-periodicity to obtain a significance (σ) for the detected quasi-periodicity.

Of the pulses selected for autocorrelation analysis, 118 pulses at 6 GHz and 24 pulses at 9 GHz had detected quasi-periodicities with significances above 4σ . The distribution of quasi-periodicities at both frequencies is shown in Figure 16. At 6 GHz, the geometric mean of the detected quasi-periodicities is 4.9 ± 1.4 ms; at 9 GHz, the mean is 7.0 ± 1.5 ms, where the $1\text{-}\sigma$ error bars are equal to the geometric standard deviation. The power-law scaling relation derived by Kramer et al. (2024) predicts a mean quasi-periodicity of 1.27 ± 0.08 ms, while the distribution of their detected quasi-periodicities had a geometric mean of 2.37 ± 0.04 ms.

The quasi-periodicities detected at 6 GHz by Kramer et al. (2024) were all shorter than 5 ms, at odds with the larger range of quasi-periodicities we observe at both frequencies. We note that at 9 GHz, many of the pulses with longer quasi-periodicities consisted of only two components separated by 5–15 ms, which would also create peaks in the ACF at a lag equal to their separation. It is likely that the combination of sub-pulse structure and the separation of discrete pulse components led

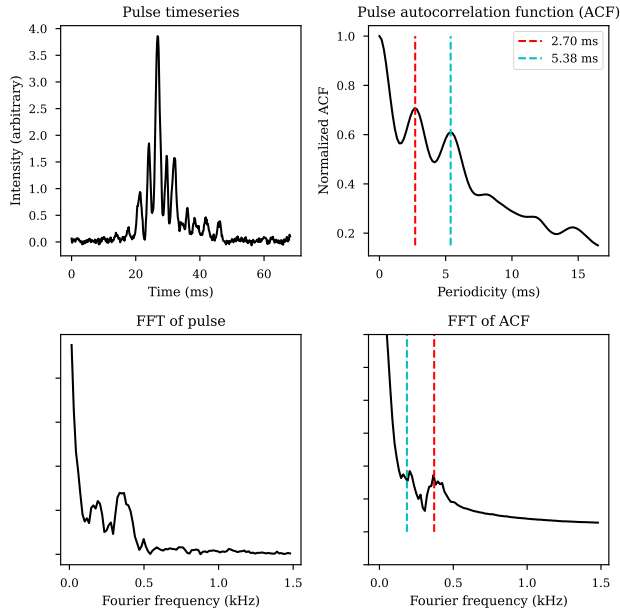


Figure 15. An example autocorrelation function analysis for a pulse at 6 GHz. Top left: pulse timeseries. Top right: pulse autocorrelation function. The identified peaks are denoted with dashed vertical lines. Bottom left: the normalized Fourier transform of the pulse timeseries. Bottom right: the normalized Fourier transform of the ACF. Vertical lines corresponding to the identified quasi-periodicities have been placed at the corresponding Fourier frequencies.

to a higher average quasi-periodicity than predicted by the scaling relation. Quasi-periodic substructure is expected to depend only on the rotational period of the neutron star, thus we do not expect that the detected quasi-periodicities will have a frequency dependence.

5. DISCUSSION AND CONCLUSIONS

5.1. The Gigahertz-Peaked Spectrum of Swift J1818.0–1607

The pulsed radio emission from magnetars tends to have a flatter spectrum than that of pulsars, allowing their detection at high observing frequencies. In this section, we discuss our measurement of steep, negative spectral indices above 9 GHz in light of the previously observed spectral properties of J1818 and other radio magnetars, and posit that J1818 exhibits radio emission with a gigahertz-peaked spectrum (GPS).

Swift J1818.0–1607 possessed a steep, negative radio spectral index ($\alpha < -1.8$) for the first few months post-outburst (Maan & van Leeuwen 2020; Lower et al. 2020), and was not detectable at or above 8 GHz (Gajjar et al. 2020; Lower & Shannon 2020). Four months post-outburst, a significant spectral flattening was detected, with a spectral index below 9 GHz of $\alpha = +0.3(2)$ (Majid et al. 2020). Follow-up observations yielded high-

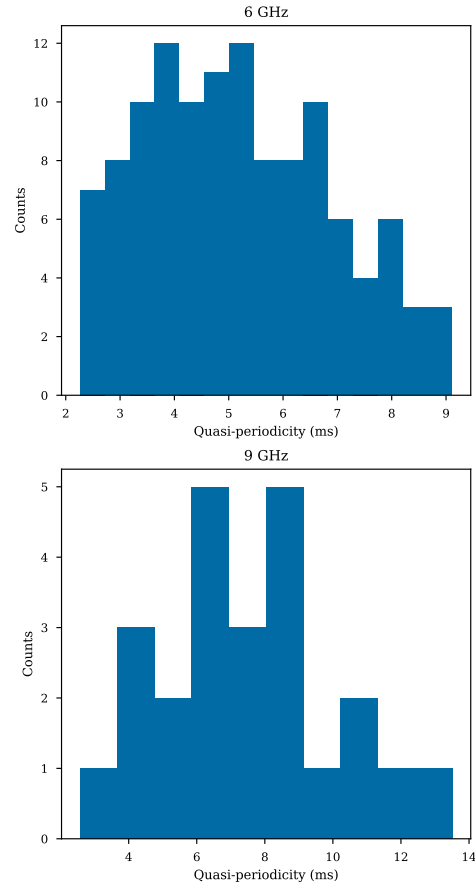


Figure 16. The distribution of detected quasi-periodicities in the single pulses of J1818 at 6 GHz (top) and 9 GHz (bottom).

frequency detections of J1818 up to 151 GHz, implying an overall flattening of the spectral index with time (Torre et al. 2020). Longer-term followup found that in the months preceding our observations, the spectral index of J1818 between 2 and 8 GHz flattened over time (Huang et al. 2021; Bansal et al. 2023).

It is not uncommon for radio magnetars, including J1818, to emit steeper-spectrum emission at radio frequencies above 10 GHz. For instance, when J1818 was first detected above 8 GHz, fitting a single power law to the flux measurements between observing bands yielded steeper, negative spectral indices (Pearlman et al. 2020; Liu et al. 2020; Torre et al. 2020). In fact, Huang et al. (2021) report an inverted spectral index ($\alpha = +0.5$) between 2 and 8 GHz on the same day that Torre et al. (2020) report a negative spectral index ($\alpha = -1.4$) between 86 and 154 GHz, leading all of the above authors to propose that J1818 exhibits a spectral turnover somewhere at high frequencies.

Based on our flux measurements (Figure 4), the flux of J1818 increases with frequency up to a peak frequency of

~ 5 GHz, before experiencing a sharp downturn. The instantaneous, in-band spectral indices of all profile components of J1818 are quite steep above 9 GHz, displaying spectral indices steeper than the average value of $\alpha = -1.6$ for radio pulsars (Jankowski et al. 2018). The clear spectral peak, and steep spectral indices at frequencies above the peak frequency, lead us to classify Swift J1818.0–1607 as having a gigahertz-peaked spectrum.

Most radio magnetars have, at least temporarily, shown evidence of radio spectra which peak at gigahertz frequencies (Gigahertz Peaked Spectrum; GPS). These include XTE J1810–197 (Eie et al. 2021), SGR 1745–2900 (Pennucci et al. 2015), 1E 1547.1–5408, and PSR J1622–4950 (Kijak et al. 2017). GPS are also observed in a very small subset of rotation-powered radio pulsars, albeit with lower peak frequencies (0.6 to 2 GHz) than the bulk of the radio magnetar population (Jankowski et al. 2018). The prevailing explanation for these spectral peaks is an interaction between the radio emission and the ionized environments around the neutron star; it is also possible that the younger magnetars are situated in denser or hotter environments, leading to higher peak frequencies (Kijak et al. 2013, 2017).

Diffuse X-ray and radio emission have been detected in the region around J1818. The X-ray emission is indicative of a dust-scattering halo, and a semi-circular region of radio emission was found surrounding the location of J1818 (Blumer & Safi-Harb 2020; Ibrahim et al. 2023). Recent VLBA astrometry has determined the proper motion and distance of J1818, and determined that their parallax distance of 9 kpc still allows for the interpretation of the diffuse radio emitting region as a potential supernova remnant association (Ding et al. 2024). This radio emitting region could contribute to the observed GPS of J1818; however, even if it is not an associated SNR, other absorbing regions along the line of sight could produce these spectral features as well (Kijak et al. 2017).

The mean flux at 35 GHz is higher than the 22-GHz flux (see Table 3), which appears counterintuitive given the relative S/N ratios of each integrated profile. At such high frequencies, weather and atmospheric effects could have enhanced the system noise at 35 GHz. Since the 35-GHz observation took place 54 days before the 22-GHz observation, it is possible that the overall flux of J1818 simply decayed in that time, or that the flux in each band varies on shorter timescales. The total spectrum shown in Figure 4 displays better continuity between the fluxes at 22 and 35 GHz, especially given the time span between observations.

Simultaneous, multi-frequency observations are necessary to determine whether spectral turnovers are present in this and other radio magnetars. If the 35-GHz flux were consistently higher than the 22-GHz flux across many observational epochs, it is possible that there is another spectral turnover and that J1818 once again exhibits a positive spectral index above 30 GHz. XTE J1810–197 exhibited similar spectral features, with a large increase in the radio flux above 150 GHz (Eie et al. 2021). The magnetars SGR 1745–1900 (Torre et al. 2017) and 1E 1547.0–5408 (Chu et al. 2021) have shown evidence of spectral turn-ups in the range of 20–80 GHz.

5.2. Pulse Profile Morphology

Across the frequency range of our observations, the integrated profiles consisted of a narrow, consistent central component (II), flanked by more sporadic components (I and III) comprised of narrow sub-pulses. The outer components tended to have flatter spectra and higher levels of modulation in time, similar to the emission properties observed in radio magnetars. Furthermore, the majority of pulses at 9 GHz with the sign of the circular polarization reversed originated from the phase range of component III only.

Early observations of J1818 found that its integrated profile typically consisted of a single peak with a high degree of linear polarization and a steep spectrum (Lower et al. 2020; Champion et al. 2020). This profile component was consistently detected across multiple epochs and frequencies, and its properties are similar to those we observe in Component II. Brighter, more sporadic pulses were occasionally detected from a postcursor component as early as five days post-outburst (Maan & van Leeuwen 2020; Champion et al. 2020), suggesting it is the same sporadic postcursor component that we observe as Component III.

We only detect the precursor component (I) with high significance at 13 and 22 GHz, the latest two observations in our dataset. 12 pulses with a significance level ≥ 4 (as defined in Section 4.1) were detected from the phase range of Component I in the 9-GHz dataset. A low S/N precursor component is visible by eye in the 35 GHz profile, though it is offset in longitude from the position of the precursor component at other frequencies.

Emission from a precursor component was also detected by Lower et al. (2021) and Huang et al. (2021). The precursor component detected at 2.5 GHz in Lower et al. (2021) seemed to appear sometime between MJDs 59009 and 59047, and over the next two months shifted in pulse longitude until it nearly overlapped the main pulse component at the end of their observations on MJD 59128. Similar drifts in the pulse longitude of indi-

vidual pulse components were also observed in the radio magnetar XTE J1810–197 (Levin et al. 2019). This component may have a sufficiently steep spectrum to not be detectable at lower frequencies, or the longitudinal drift may have reversed direction between observations.

Huang et al. (2021) took simultaneous 2.25- and 8.6-GHz observations of J1818, which ran from MJD 58936 until MJD 59092 (the date of our first observation). In these observations, the middle component is consistent in time and generally narrower at 8.6 GHz than at 2.2 GHz, and the flanking profile components tend to be wider and more sporadic than the middle component.

5.2.1. Pulse Widths

Many rotation-powered pulsars display narrower pulse widths at higher observing frequencies (Pilia et al. 2016). Pulse width narrowing with increasing frequency was also observed in the case of the magnetar XTE J1810–197 (Eie et al. 2021). The evolution of pulse width with observing frequency in canonical pulsars is explained with radius-frequency mapping (RFM), which predicts that pulse widths narrow at higher radio frequencies (Cordes 1978). The FWHM of the main component of the integrated profile remains mostly consistent across our observing frequencies, yet significantly broadens between 22 and 35 GHz (see Table 2). Simultaneous, multi-frequency observations would be necessary in order to determine whether these variations are frequency- or epoch-dependent.

5.2.2. Mode Switching

We find that over the course of our observations, the integrated pulse profile of Swift J1818.0–1607 was quite stable at all observing frequencies on timescales of minutes. J1818 has previously exhibited mode changing behavior, alternating between quasi-stable emission states on timescales of minutes, but only very occasionally. J1818 seemed to enter a period of enhanced mode-changing activity between 2020 June and 2020 August, when mode switching was observed at frequencies of 1.4 GHz (Rajwade et al. 2022), and simultaneously at 2.2 and 8.5 GHz (Huang et al. 2021; Bansal et al. 2023). Lower et al. (2020) also observe two distinct types of mode switching below 4 GHz, on minutes-long timescales, though the modes have different emission properties than the modes seen in the other studies.

Mode switching is often explained by changes in the large-scale configuration of the pulsar magnetosphere (Timokhin 2010). Given our lack of detection of any kind of mode switching in our observations, it is possible that J1818 settled into a more stable emission state roughly five months post-outburst.

5.3. Single Pulse Properties

5.3.1. Pulse Energies

The Crab pulsar, among other pulsars, has been observed to emit giant pulses, usually defined as having a flux above 10 times the average pulse flux; pulse amplitude distributions containing giant pulses are best fit with a power-law tail (Mickaliger et al. 2012). On the other hand, the pulse energy distributions of many standard pulsars follow a log-normal distribution, with no high-energy tail (Burke-Spolaor et al. 2012). Comparisons in the pulse energy distributions of rotating radio transients (RRATs) and standard pulsars have also been used to clarify their emission mechanisms (Cui et al. 2017; Mickaliger et al. 2018).

The log-normal distribution provides a better fit for the observations at 820 MHz, 6 GHz, and 9 GHz. At 13 and 22 GHz, the log-normal fits underestimate the number of pulses with fluxes $\gtrsim 1.5$ times the average flux; however, the small number of pulses in many of the high-flux bins make the use of the chi-squared test less accurate. Given that the normalized fluxes at these frequencies do not surpass five times the average peak flux density, they are likely not created by a giant pulse emission mechanism as seen in other pulsars, e.g. the Crab.

The only pulses resembling giant pulses in our sample are some bright pulses from Component III at 6 GHz. Though these pulses surpass the criterion of a pulse energy ≥ 10 times the average energy, at higher frequencies, no pulses pass this threshold, and the power-law fit only outperforms a log-normal fit at 6 and 9 GHz. Interestingly, the pulse energy distributions from Component II are better fit by power law distributions than log-normal distributions, except for at 9 GHz where the model slightly overfits the data (e.g., $\chi_r^2 < 1$). In all other regards, the central component has tended to display more pulsar-like characteristics, so it would be a reasonable expectation that the log-normal fits would be preferred for the central component’s energy distributions.

The pulse energy distributions of the Galactic center magnetar SGR J1745–2900 have been well-fit by log-normal distributions before (Lynch et al. 2015; Yan et al. 2018). A similar lack of a high-energy tail from the single pulses of J1818 was observed by Lower et al. (2020), and Champion et al. (2020) detected only one pulse with an energy > 10 times the average, a few weeks after outburst. A study of pulse energy distributions from the magnetar XTE J1810–197 between 1–8 GHz found that the energies are not well-described by a single statistical distribution, and varied on timescales of days (Serylak et al. 2009).

5.3.2. Frequency Structure

Other radio magnetar studies have found frequency structure in magnetar bursts, similar to fast radio bursts (Pearlman et al. 2018; Maan et al. 2019). In these cases, individual sub-pulses within a magnetar rotation would have flux densities which varied by factors of 2–10 across the observing band, as well as the radio emission disappearing over ~ 100 -MHz wide intervals in the observing band. As exemplified in Figure 6, the single pulses from our observations of J1818 displayed broadband emission, and we did not observe narrowband frequency structure in our single pulses, nor did we observe the downward drifting frequency behavior in subsequent subpulses often seen in repeating FRBs. Maan et al. (2019) showed that in the case of XTE J1810–197, high degrees of frequency modulation were more common closer to the beginning of the outburst, and that the frequency structure of the magnetar single pulses tended to be more uniform at later observing dates.

6. CONCLUSIONS

We carried out observations of the radio magnetar Swift J1818.0–1607 with the GBT over a range of frequencies from 0.8 to 35 GHz beginning five months after its March 2020 outburst. At observing frequencies above 6 GHz, the spectral index of the radio emission overturns and significantly steepens, indicating that J1818 at least temporarily exhibited a gigahertz-peaked spectrum (GPS) commonly seen in radio magnetars. A potential supernova remnant has previously been identified in the region around J1818 in the form of a semi-circular radio-emitting region and extended dust-scattering X-ray halo, which could cause the observed GPS.

The integrated pulse profile of J1818 was also remarkably stable across frequencies, consisting of up to three pulse components. The central component (Component II) tends to be narrower and displays less flux variability over time when compared to the other two compo-

nents. The postcursor (Component III) in particular is composed largely of narrow, bright subpulses which fall within the larger pulse envelope, reminiscent of the highly variable radio bursts from magnetars. At most frequencies, the outer profile components have flatter spectral indices and higher flux modulation indices than the central component.

We did not observe FRB-like behavior from J1818 in these observations, namely, narrowband pulses with downward-drifting frequency structure, nor pulses with sufficient energies to be detected as FRBs had J1818 been more distant. Given the stable pulse profile across observing epochs and frequencies, and the lack of mode changing on short timescales, the magnetosphere of J1818 may have settled to a more stable configuration in the months following its initial outburst.

E.F.L. and M.A.M. are supported by NSF award AST-2009425. M.A.M. is also supported by NSF Physics Frontiers Center award PHYS-2020265. The Green Bank Observatory is a facility of the National Science Foundation operated under cooperative agreement by Associated Universities, Inc.

Facilities: GBT (VEGAS)

Software: **Astropy** (<https://www.astropy.org/>; Astropy Collaboration et al. 2022), **Matplotlib** (<https://matplotlib.org/>; Hunter 2007), **Numpy** (<https://numpy.org/>; Harris et al. 2020), **PRESTO** (<https://www.cv.nrao.edu/~sransom/presto/>; Ransom 2001), **PSRCHIVE** (<https://psrchive.sourceforge.net/>; Hotan et al. 2004; van Straten et al. 2011), **pypulse** (<https://github.com/mtlam/PyPulse>; Lam 2017), **pyGDSM** (<https://github.com/telegraphic/pygds>; Price 2016), **Scipy** (<https://scipy.org/>; Virtanen et al. 2020), **seaborn** (<https://github.com/mwaskom/seaborn>; Waskom 2021), **TEMPO2** (<https://www.atnf.csiro.au/research/pulsar/tempo2/>; Hobbs et al. 2006)

REFERENCES

- Archibald, R. F., Kaspi, V. M., Tendulkar, S. P., & Scholz, P. 2016, *ApJL*, 829, L21, doi: [10.3847/2041-8205/829/1/L21](https://doi.org/10.3847/2041-8205/829/1/L21)
- Astropy Collaboration, Price-Whelan, A. M., Lim, P. L., et al. 2022, *ApJ*, 935, 167, doi: [10.3847/1538-4357/ac7c74](https://doi.org/10.3847/1538-4357/ac7c74)
- Bansal, K., Wharton, R. S., Pearlman, A. B., et al. 2023, *MNRAS*, 523, 2401, doi: [10.1093/mnras/stad1520](https://doi.org/10.1093/mnras/stad1520)
- Blumer, H., & Safi-Harb, S. 2020, *ApJL*, 904, L19, doi: [10.3847/2041-8213/abc6a2](https://doi.org/10.3847/2041-8213/abc6a2)
- Bochenek, C. D., Ravi, V., Belov, K. V., et al. 2020, *Nature*, 587, 59, doi: [10.1038/s41586-020-2872-x](https://doi.org/10.1038/s41586-020-2872-x)
- Burke-Spolaor, S., Johnston, S., Bailes, M., et al. 2012, *MNRAS*, 423, 1351, doi: [10.1111/j.1365-2966.2012.20998.x](https://doi.org/10.1111/j.1365-2966.2012.20998.x)
- Camilo, F., Ransom, S. M., Halpern, J. P., et al. 2016, *ApJ*, 820, 110, doi: [10.3847/0004-637X/820/2/110](https://doi.org/10.3847/0004-637X/820/2/110)
- Champion, D., Cognard, I., Cruces, M., et al. 2020, *MNRAS*, 498, 6044, doi: [10.1093/mnras/staa2764](https://doi.org/10.1093/mnras/staa2764)

- CHIME/FRB Collaboration, Andersen, B. C., Bandura, K. M., et al. 2020, *Nature*, 587, 54, doi: [10.1038/s41586-020-2863-y](https://doi.org/10.1038/s41586-020-2863-y)
- Chu, C.-Y., Ng, C. Y., Kong, A. K. H., & Chang, H.-K. 2021, *MNRAS*, 503, 1214, doi: [10.1093/mnras/stab349](https://doi.org/10.1093/mnras/stab349)
- Cordes, J. M. 1978, *ApJ*, 222, 1006, doi: [10.1086/156218](https://doi.org/10.1086/156218)
- Cordes, J. M., & Lazio, T. J. W. 2002, arXiv e-prints, astro. <https://arxiv.org/abs/astro-ph/0207156>
- Cui, B. Y., Boyles, J., McLaughlin, M. A., & Palliyaguru, N. 2017, *ApJ*, 840, 5, doi: [10.3847/1538-4357/aa6aa9](https://doi.org/10.3847/1538-4357/aa6aa9)
- Dai, S., Johnston, S., Weltevrede, P., et al. 2018, *MNRAS*, 480, 3584, doi: [10.1093/mnras/sty2063](https://doi.org/10.1093/mnras/sty2063)
- Dai, S., Lower, M. E., Bailes, M., et al. 2019, *ApJL*, 874, L14, doi: [10.3847/2041-8213/ab0e7a](https://doi.org/10.3847/2041-8213/ab0e7a)
- Ding, H., Lower, M. E., Deller, A. T., et al. 2024, *ApJL*, 971, L13, doi: [10.3847/2041-8213/ad5550](https://doi.org/10.3847/2041-8213/ad5550)
- Duncan, R. C., & Thompson, C. 1992, *ApJL*, 392, L9, doi: [10.1086/186413](https://doi.org/10.1086/186413)
- Eie, S., Terasawa, T., Akahori, T., et al. 2021, *PASJ*, 73, 1563, doi: [10.1093/pasj/psab098](https://doi.org/10.1093/pasj/psab098)
- Enoto, T., Sakamoto, T., Younes, G., et al. 2020, *The Astronomer's Telegram*, 13551, 1
- Evans, P. A., Gropp, J. D., Kennea, J. A., et al. 2020, *GRB Coordinates Network*, 27373, 1
- Gajjar, V., Perez, K., Siemion, A., et al. 2020, *The Astronomer's Telegram*, 13575, 1
- Harris, C. R., Millman, K. J., van der Walt, S. J., et al. 2020, *Nature*, 585, 357, doi: [10.1038/s41586-020-2649-2](https://doi.org/10.1038/s41586-020-2649-2)
- Hobbs, G. B., Edwards, R. T., & Manchester, R. N. 2006, *MNRAS*, 369, 655, doi: [10.1111/j.1365-2966.2006.10302.x](https://doi.org/10.1111/j.1365-2966.2006.10302.x)
- Hotan, A. W., van Straten, W., & Manchester, R. N. 2004, *PASA*, 21, 302, doi: [10.1071/AS04022](https://doi.org/10.1071/AS04022)
- Hu, C.-P., Begiçarslan, B., Güver, T., et al. 2020, *ApJ*, 902, 1, doi: [10.3847/1538-4357/abb3c9](https://doi.org/10.3847/1538-4357/abb3c9)
- Huang, Z.-P., Yan, Z., Shen, Z.-Q., et al. 2021, *MNRAS*, 505, 1311, doi: [10.1093/mnras/stab1362](https://doi.org/10.1093/mnras/stab1362)
- Hunter, J. D. 2007, *Computing in Science & Engineering*, 9, 90, doi: [10.1109/MCSE.2007.55](https://doi.org/10.1109/MCSE.2007.55)
- Ibrahim, A. Y., Borghese, A., Rea, N., et al. 2023, *ApJ*, 943, 20, doi: [10.3847/1538-4357/aca528](https://doi.org/10.3847/1538-4357/aca528)
- Jankowski, F., van Straten, W., Keane, E. F., et al. 2018, *MNRAS*, 473, 4436, doi: [10.1093/mnras/stx2476](https://doi.org/10.1093/mnras/stx2476)
- Karuppusamy, R., Desvignes, G., Kramer, M., et al. 2020, *The Astronomer's Telegram*, 13553, 1
- Kaspi, V. M., & Beloborodov, A. M. 2017, *ARA&A*, 55, 261, doi: [10.1146/annurev-astro-081915-023329](https://doi.org/10.1146/annurev-astro-081915-023329)
- Kijak, J., Basu, R., Lewandowski, W., & Rożko, K. 2021, *ApJ*, 923, 211, doi: [10.3847/1538-4357/ac3082](https://doi.org/10.3847/1538-4357/ac3082)
- Kijak, J., Basu, R., Lewandowski, W., Rożko, K., & Dembska, M. 2017, *ApJ*, 840, 108, doi: [10.3847/1538-4357/aa6ff2](https://doi.org/10.3847/1538-4357/aa6ff2)
- Kijak, J., Tarczewski, L., Lewandowski, W., & Melikidze, G. 2013, *ApJ*, 772, 29, doi: [10.1088/0004-637X/772/1/29](https://doi.org/10.1088/0004-637X/772/1/29)
- Kramer, M., Liu, K., Desvignes, G., Karuppusamy, R., & Stappers, B. W. 2024, *Nature Astronomy*, 8, 230, doi: [10.1038/s41550-023-02125-3](https://doi.org/10.1038/s41550-023-02125-3)
- Kramer, M., Stappers, B. W., Jessner, A., Lyne, A. G., & Jordan, C. A. 2007, *MNRAS*, 377, 107, doi: [10.1111/j.1365-2966.2007.11622.x](https://doi.org/10.1111/j.1365-2966.2007.11622.x)
- Lam, M. T. 2017, *PyPulse: PSRFITS handler*, Astrophysics Source Code Library, record ascl:1706.011
- Levin, L., Bailes, M., Bates, S. D., et al. 2012, *MNRAS*, 422, 2489, doi: [10.1111/j.1365-2966.2012.20807.x](https://doi.org/10.1111/j.1365-2966.2012.20807.x)
- Levin, L., Lyne, A. G., Desvignes, G., et al. 2019, *MNRAS*, 488, 5251, doi: [10.1093/mnras/stz2074](https://doi.org/10.1093/mnras/stz2074)
- Liu, K., Karuppusamy, R., Cognard, I., et al. 2020, *The Astronomer's Telegram*, 13997, 1
- Lorimer, D. R., & Kramer, M. 2012, *Handbook of Pulsar Astronomy*
- Lower, M. E., Johnston, S., Shannon, R. M., Bailes, M., & Camilo, F. 2021, *MNRAS*, 502, 127, doi: [10.1093/mnras/staa3789](https://doi.org/10.1093/mnras/staa3789)
- Lower, M. E., & Shannon, R. M. 2020, *The Astronomer's Telegram*, 13587, 1
- Lower, M. E., Shannon, R. M., Johnston, S., & Bailes, M. 2020, *ApJL*, 896, L37, doi: [10.3847/2041-8213/ab9898](https://doi.org/10.3847/2041-8213/ab9898)
- Lower, M. E., Younes, G., Scholz, P., et al. 2023, *ApJ*, 945, 153, doi: [10.3847/1538-4357/acbc7c](https://doi.org/10.3847/1538-4357/acbc7c)
- Lynch, R. S., Archibald, R. F., Kaspi, V. M., & Scholz, P. 2015, *ApJ*, 806, 266, doi: [10.1088/0004-637X/806/2/266](https://doi.org/10.1088/0004-637X/806/2/266)
- Maan, Y., Joshi, B. C., Surnis, M. P., Bagchi, M., & Manoharan, P. K. 2019, *ApJL*, 882, L9, doi: [10.3847/2041-8213/ab3a47](https://doi.org/10.3847/2041-8213/ab3a47)
- Maan, Y., & van Leeuwen, J. 2020, *The Astronomer's Telegram*, 13560, 1
- Majid, W. A., Pearlman, A. B., Prince, T. A., Naudet, C. J., & Bansal, K. 2020, *The Astronomer's Telegram*, 13898, 1
- Men, Y., McSweeney, S., Hurley-Walker, N., Barr, E., & Stappers, B. 2025, arXiv e-prints, arXiv:2501.10528, doi: [10.48550/arXiv.2501.10528](https://doi.org/10.48550/arXiv.2501.10528)
- Mickaliger, M. B., McEwen, A. E., McLaughlin, M. A., & Lorimer, D. R. 2018, *MNRAS*, 479, 5413, doi: [10.1093/mnras/sty1785](https://doi.org/10.1093/mnras/sty1785)
- Mickaliger, M. B., McLaughlin, M. A., Lorimer, D. R., et al. 2012, *ApJ*, 760, 64, doi: [10.1088/0004-637X/760/1/64](https://doi.org/10.1088/0004-637X/760/1/64)

- Pearlman, A. B., Majid, W. A., Prince, T. A., Kocz, J., & Horiuchi, S. 2018, *ApJ*, 866, 160, doi: [10.3847/1538-4357/aade4d](https://doi.org/10.3847/1538-4357/aade4d)
- Pearlman, A. B., Majid, W. A., Prince, T. A., et al. 2020, *The Astronomer's Telegram*, 13966, 1
- Pennucci, T. T., Possenti, A., Esposito, P., et al. 2015, *ApJ*, 808, 81, doi: [10.1088/0004-637X/808/1/81](https://doi.org/10.1088/0004-637X/808/1/81)
- Pilia, M., Hessels, J. W. T., Stappers, B. W., et al. 2016, *A&A*, 586, A92, doi: [10.1051/0004-6361/201425196](https://doi.org/10.1051/0004-6361/201425196)
- Price, D. C. 2016, *PyGDSM: Python interface to Global Diffuse Sky Models*, *Astrophysics Source Code Library*, record ascl:1603.013
- Radhakrishnan, V., & Cooke, D. J. 1969, *Astrophys. Lett.*, 3, 225
- Rajwade, K., Stappers, B., Lyne, A., et al. 2020, *The Astronomer's Telegram*, 13554, 1
- Rajwade, K. M., Stappers, B. W., Lyne, A. G., et al. 2022, *MNRAS*, 512, 1687, doi: [10.1093/mnras/stac446](https://doi.org/10.1093/mnras/stac446)
- Ransom, S. M. 2001, PhD thesis, Harvard University
- Scholz, P., Camilo, F., Sarkissian, J., et al. 2017, *ApJ*, 841, 126, doi: [10.3847/1538-4357/aa73de](https://doi.org/10.3847/1538-4357/aa73de)
- Serylak, M., Stappers, B. W., Weltevrede, P., et al. 2009, *MNRAS*, 394, 295, doi: [10.1111/j.1365-2966.2008.14260.x](https://doi.org/10.1111/j.1365-2966.2008.14260.x)
- Stamatikos, M., Barthelmy, S. D., Cummings, J. R., et al. 2020, *GRB Coordinates Network*, 27384, 1
- Timokhin, A. N. 2010, *MNRAS*, 408, L41, doi: [10.1111/j.1745-3933.2010.00924.x](https://doi.org/10.1111/j.1745-3933.2010.00924.x)
- Torne, P., Eatough, R. P., Karuppusamy, R., et al. 2015, *MNRAS*, 451, L50, doi: [10.1093/mnrasl/slv063](https://doi.org/10.1093/mnrasl/slv063)
- Torne, P., Desvignes, G., Eatough, R. P., et al. 2017, *MNRAS*, 465, 242, doi: [10.1093/mnras/stw2757](https://doi.org/10.1093/mnras/stw2757)
- Torne, P., Liu, K., Cognard, I., et al. 2020, *The Astronomer's Telegram*, 14001, 1
- Torne, P., Bell, G. S., Bintley, D., et al. 2022, *ApJL*, 925, L17, doi: [10.3847/2041-8213/ac4caa](https://doi.org/10.3847/2041-8213/ac4caa)
- van Straten, W., Demorest, P., Khoo, J., et al. 2011, *PSRCHIVE: Development Library for the Analysis of Pulsar Astronomical Data*, *Astrophysics Source Code Library*, record ascl:1105.014. <http://ascl.net/1105.014>
- Virtanen, P., Gommers, R., Oliphant, T. E., et al. 2020, *Nature Methods*, 17, 261, doi: [10.1038/s41592-019-0686-2](https://doi.org/10.1038/s41592-019-0686-2)
- Wahl, H. M., McLaughlin, M. A., Gentile, P. A., et al. 2022, *ApJ*, 926, 168, doi: [10.3847/1538-4357/ac4045](https://doi.org/10.3847/1538-4357/ac4045)
- Waskom, M. 2021, *The Journal of Open Source Software*, 6, 3021, doi: [10.21105/joss.03021](https://doi.org/10.21105/joss.03021)
- Weltevrede, P., Edwards, R. T., & Stappers, B. W. 2006, *A&A*, 445, 243, doi: [10.1051/0004-6361:20053088](https://doi.org/10.1051/0004-6361:20053088)
- Yan, W. M., Wang, N., Manchester, R. N., Wen, Z. G., & Yuan, J. P. 2018, *MNRAS*, 476, 3677, doi: [10.1093/mnras/sty470](https://doi.org/10.1093/mnras/sty470)
- Yao, J. M., Manchester, R. N., & Wang, N. 2017, *ApJ*, 835, 29, doi: [10.3847/1538-4357/835/1/29](https://doi.org/10.3847/1538-4357/835/1/29)
- Zheng, H., Tegmark, M., Dillon, J. S., et al. 2017, *MNRAS*, 464, 3486, doi: [10.1093/mnras/stw2525](https://doi.org/10.1093/mnras/stw2525)